



Contents lists available at ScienceDirect

International Journal of Rock Mechanics and Mining Sciences

journal homepage: <http://www.elsevier.com/locate/ijrmms>

# Hydromechanical properties of 3D printed fractures with controlled surface roughness: Insights into shear-permeability coupling processes

Takuya Ishibashi<sup>a,\*</sup>, Yi Fang<sup>b</sup>, Derek Elsworth<sup>c</sup>, Noriaki Watanabe<sup>d</sup>, Hiroshi Asanuma<sup>a</sup>

<sup>a</sup> Fukushima Renewable Energy Institute, National Institute of Advanced Industrial Science and Technology, 2-2-9, Machiike-dai, Koriyama, Fukushima, 963-0298, Japan

<sup>b</sup> Institute for Geophysics, Jackson School of Geosciences, The University of Texas at Austin, Austin, TX, USA

<sup>c</sup> Department of Energy and Mineral Engineering, EMS Energy Institute, And G3 Center, The Pennsylvania State University, University Park, PA, USA

<sup>d</sup> Graduate School of Environmental Studies, Tohoku University, 6-6-20 Aramaki-aza-Aoba, Aoba-ku, Sendai, 980-8579, Japan

## ARTICLE INFO

### Keywords:

3D printer/printing  
Rock fracture  
Surface roughness  
Shear dilation  
Experimental reproducibility

## ABSTRACT

We explore the potentials of three-dimensional (3D) printing to explore hydromechanical processes in laboratory-scale fractures. 3D printing enables replication of designer fractures with quantified and repeatable roughness to examine the interdependencies between mechanical and hydraulic response including, for example, the Barton-Bandis model. The present study successfully probes subtle variations of shear strength and dilation behavior in 3D printed fractures controlled by surface roughness. For constant materials and basic frictional characteristics, shear strength increases with increasing the standard deviation of the surface height with dilation rate principally controlled by the average amplitude of the long period wavelength of the fracture surface and insensitive the secondary (minor amplitude) roughness. Importantly, these sensitivities are manifest in the permeability response. With increasing shear displacement, the fracture permeability first decreases and then increases with oscillations resulting from step changes in fracture-fracture contact architectures. As these distinctive behaviors are consistent with those of real rock fractures, we conclude that 3D printed fractures provide a useful analog to real rock fractures when constraining slip-permeability coupling during shear slip.

## 1. Introduction

Coupled interaction between mechanical and hydraulic processes in rock fractures are of significance in various engineering applications, for example, in determining hydraulic stimulation protocols (fracturing versus shearing) in hydrocarbon and geothermal reservoirs. From a scientific perspective, it also contributes to understanding reactivation mechanisms of natural faults.<sup>1,2</sup> Natural rock fractures/faults are rough and fracture surface roughness and associated heterogeneity of aperture distributions significantly impact hydromechanical processes.<sup>3,4</sup> More specifically, it is well known that the hydromechanical parameters, such as peak shear strength, friction/dilation angle, aperture, permeability change, and their relationships are significantly influenced by the surface roughness<sup>5-7</sup> with these studies originating from the work of Barton et al. (1985)<sup>8</sup> and Maini (1971).<sup>9</sup> To achieve more realistic simulations of hydraulic fracturing, and in understanding induced or repeated earthquakes, it is vital to accurately constrain the constitutive relations

defining the slip-dependent evolution of hydromechanical parameters.

In conducting systematic studies on rock fractures with surface roughness, one significant difficulty is that the role of surface roughness of natural rock fractures/faults in influencing their hydromechanical properties cannot be systematically isolated and controlled. This challenge is due to the fact that surface roughness of natural rock fractures/faults is specified as a consequence of the combination of rock type, crustal stress, and associated tectonic history.<sup>10</sup> As the Barton-Bandis model<sup>8</sup> and its derivative models, which link the hydromechanical response to surface roughness, are empirical, some innovative approaches are necessary to define a process-based model of response. Thus, we use 3D printing to replicate repeatable numerically designed “designer” rough fractures<sup>3</sup> to achieve such model refinement and to investigate in detail the contributing and controlling physical processes.

3D printing is being actively applied in the geosciences and in ge-engineering<sup>11-13</sup> spurred by recent advances in non-destructive technology and digital rock physics. Different from real rock specimens, 3D

\* Corresponding author.

E-mail addresses: [takuya.ishibashi@aist.go.jp](mailto:takuya.ishibashi@aist.go.jp) (T. Ishibashi), [yi.fang@utexas.edu](mailto:yi.fang@utexas.edu) (Y. Fang), [elsworth@psu.edu](mailto:elsworth@psu.edu) (D. Elsworth), [noriaki.watanabe.e6@tohoku.ac.jp](mailto:noriaki.watanabe.e6@tohoku.ac.jp) (N. Watanabe), [h.asanuma@aist.go.jp](mailto:h.asanuma@aist.go.jp) (H. Asanuma).

<https://doi.org/10.1016/j.ijrmms.2020.104271>

Received 8 July 2019; Received in revised form 16 January 2020; Accepted 19 February 2020

Available online 29 February 2020

1365-1609/© 2020 Elsevier Ltd. All rights reserved.

printing makes it easy to design/control the internal void/micro-fractures structure or heterogeneous distribution of aperture and to repeatedly prepare the specimens having exactly the same geometrical features and with very high accuracy. The accuracy of reproducing 3D samples depends on the printing methods (inkjet, powder bonding, stereolithography etc.) and is generally within the range 0.02 mm–0.2 mm. Thus, 3D printing has been used to assess the influences of internal porous/micro fracture architecture on the bulk transport properties of rock.<sup>11,12</sup> Importantly, the macroscopic brittleness and associated failure behavior sometimes can be comparable to those of real rocks,<sup>14–16</sup> and the direct visualization/analysis of fracture-propagation/asperity-degradation processes may be realized by introducing novel visualizing techniques.<sup>17</sup> Conversely, the absolute magnitude of representative mechanical parameters (Young's modulus and Uniaxial compression strength (UCS)) of 3D printed materials, regardless of whether they are ceramics, gypsum, artificial sandstone or resin, are still much smaller than those of real rocks (see Kong et al. (2018) and Zhou and Zhu (2018) for detailed comparisons),<sup>14–16</sup> and further improvements and development of 3D printing materials and methods are needed to fill this gap. Thus, in applying 3D printing in rock mechanics, it is important to be fully aware of the aforementioned advantages and limitations.

This study explores the potentials of 3D printing to probe key hydromechanical processes and feedbacks in laboratory-scale fractures. Numerically designed 3D printed fractures are first prepared with systematically controlled surface roughness. These are then used for direct-shear experiments to evaluate the slip-dependent changes of hydromechanical parameters. Finally, by comparing the experimental results of 3D printed fractures with those of natural rock fractures, we discuss the possibility of using 3D printed fractures as a substitute for real rock fractures.

## 2. Experimental method

### 2.1. Preparation of 3D printed fractures

We utilize the methods of Brown et al. (1995)<sup>18</sup> and Glover et al. (1998)<sup>19</sup> to numerically create self-similar surface topographies of fractures with controlled combinations of fractal dimension ( $D$ ) and standard deviation ( $s$ ) of the surface height (see also Power et al. (1987)<sup>20</sup> for a detailed discussion). Surface topographies of rectangular fractures, 19 mm in width and 38 mm in length, are numerically created on a  $100\ \mu\text{m} \times 100\ \mu\text{m}$  square grid (i.e.,  $190 \times 380$  data points).  $D$  is set to 1.1, 1.3, and 1.5, and three different values of  $s$  are considered for each case. Thus, we use a total of 9 surface topographies in this study (Table 1). These combinations of  $D$  and  $s$  are set with reference to measurements for an artificially created tensile fracture in granite.<sup>3</sup> Surface topographies are shown in Fig. 1a, and the representative scan lines, which cross at  $y = 10\ \text{mm}$  (e.g., the gray line #1 of Fig. 1a), for each surface topography are also shown in Fig. 1b. Moreover, the

**Table 1**

Parameter set for fracture shearing experiments with 3D printed fracture samples.

Sample No.	Fractal dimension [–]	Standard deviation [mm]	Shear strength (Peak) [–]	Displacement at peak strength [mm]	Shear strength (Post peak) [–]
#01	1.1	0.25	N/A	N/A	N/A
#02	1.1	0.31	N/A	N/A	N/A
#03	1.1	0.39	N/A	N/A	N/A
#04	1.3	0.37	N/A	N/A	N/A
#05	1.3	0.41	0.62	1.57	0.55
#06	1.3	0.48	0.92	1.29	0.74
#07	1.5	0.42	0.63	1.19	0.51
#08	1.5	0.56	0.77	1.3	0.68
#09	1.5	0.72	0.77	1.3	0.64

relationship between  $D$  and  $s$  is summarized in Fig. 1c, identifying that these roughness parameters are systematically controlled in this study. As briefly described in Fig. 1, a lower  $D$  value results in a flatter slope – see the linear relationship between power spectral density (PSD) and spatial frequency. Conversely, reducing  $s$  corresponds to shifting the self-similar linear relationship downward on the graph, and results in a decrease in the maximum elevation difference peak-to-trough.

By using these surface topography data, the rectangular parallelepiped sample (19 mm width, 38 mm length, and 11 mm height) with a single fracture at the center is subsequently digitally designed in STL (Stereolithography) format. The rectangular parallelepiped sample consists of two separated blocks with identical fracture surface topography. These STL format data are then read by the 3D printer (AGILISTA-3100 (Keyence) at Fukushima Renewable Energy Institute, AIST) to repeatably fabricate solid coupons (Fig. 2a) that conform to the central design. The 3D printer adopts an inkjet printing method, enabling high-precision replication with a horizontal (x-y plane) resolution of  $635 \times 400\ \text{dpi}$  (i.e.,  $40\ \mu\text{m} \times 63.5\ \mu\text{m}$ ) and a vertical (height - z direction) resolution of  $15\ \mu\text{m}$ . These values are comparable to those of previous studies.<sup>11,12</sup> Then, we print 9 sets of interlocking fracture samples with controlled rough surfaces (e.g. Fig. 2b). The printing material is ultraviolet curable acrylic resin with physical properties summarized in Table 2. These parameters are obtained based on the standard tests in Japan (e.g., JIS K7161, JIS K7171, JIS K7181, and so on) and are listed in the manufacture's catalog. Since the ultraviolet curing procedure (i.e., irradiation strength/time) is automatically and repeatably controlled by the 3D printer, the resin hardening process is standardized between samples and its impact on physical properties is negligible – the samples are true replicates. Table 2 indicates that the Young's modulus and compressive strength are much smaller, and tensile strength are much larger than those of typical rock, say granite. Based on these values, the normal and shear stiffnesses of the 3D printed fractures are further evaluated to be smaller than those typical of fractures in rock. Thus, the use of 3D printed fractures should be limited to the low stress conditions. Such limitations in the experimental similitude and representativeness of 3D printed samples in representing rock media has also been reported in Kong et al. (2018)<sup>16</sup> and Zhou and Zhu (2018).<sup>14</sup> Further advances in 3D printing technology may indeed address and ameliorate these issues. The 3D printed samples prepared in such a manner are mounted in a triaxial cell to concurrently measure the evolution of shear strength and fracture permeability evolution during shearing (Fig. 2c).<sup>2</sup>

### 2.2. Experimental apparatus and experimental procedure

The experimental apparatus (Fig. 2c) independently controls confining pressure, pore pressure, and shear velocity via three syringe pumps (500D, TELEDYNE ISCO), and can also monitor the evolution of shear strength and fracture permeability concurrent with shear. Shear displacement is additionally monitored using the linear variable differential transformer (LVDT) mounted outside the pressure vessel. We first pack the 3D printed sample within a pair of steel shearing platens, which are then jacketed within a latex membrane to isolate the sample and internal pore pressure from the confining fluid.<sup>2</sup> Note that the gap in the platens-offset and the gap at lateral sides of platens are filled with highly-deformable material to prevent the intrusion of confining fluid into the platens-offset gap and to seal against potential short circuiting of fluid flow along the lateral sides of the platens. The mechanical effect of the deformable material has been calibrated out by measuring its effect on a fracture sample with low/zero friction coefficient (e.g., fractures with Teflon-coated surfaces). All experiments are performed at room temperature (25 °C). During the experiment, we record pressure, flow rate, and evolving volume of the three syringe pumps and the shear displacement at a sampling rate of 2 Hz. As long as the syringe pump controlling the confining pressure is set to constant pressure mode, the change in the remaining volume of the pump nearly corresponds to the change in aperture volume within the fracture due to the shear

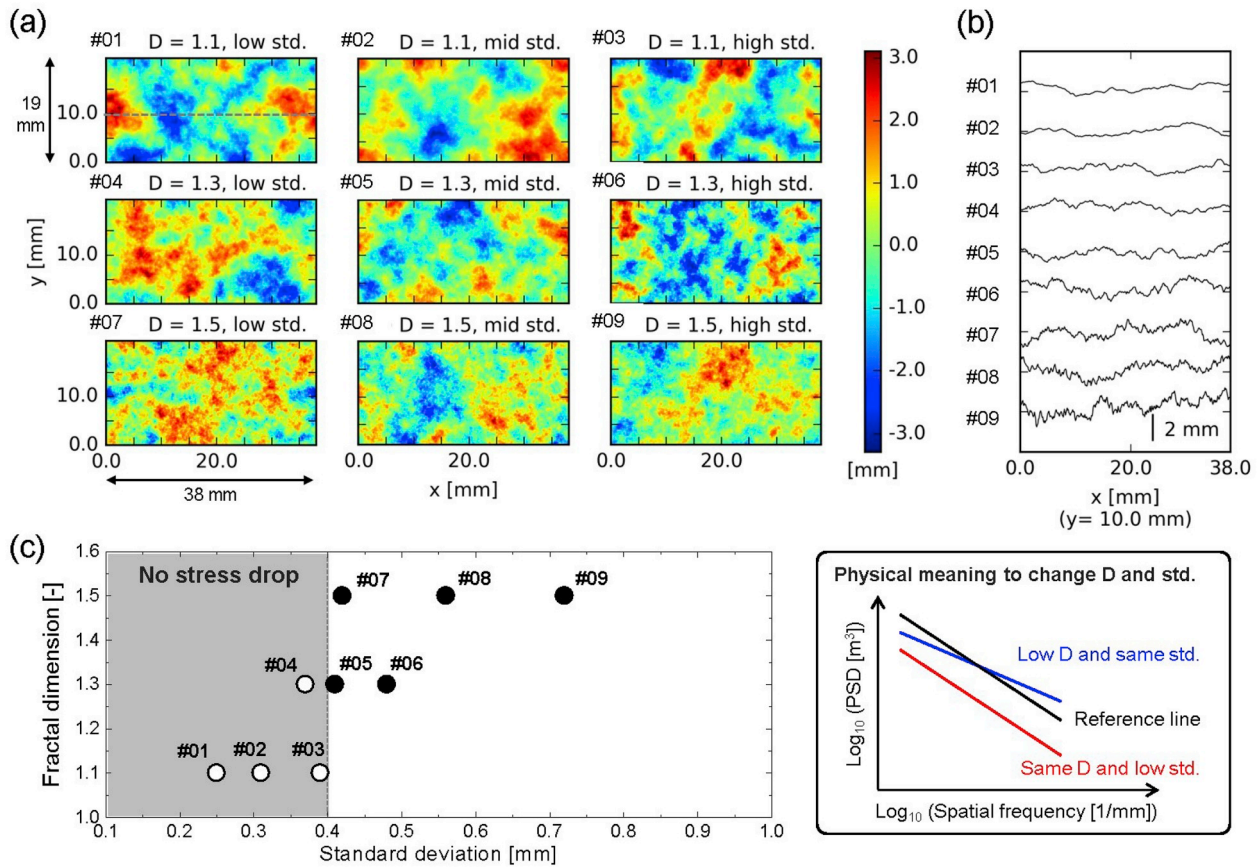


**Fig. 1.** (a) Surface topographies with various combinations of fractal dimension and standard deviation for surface height, (b) representative scan lines for each surface topography, and (c) change in fractal dimension,  $D$ , and standard deviation,  $s$ , for surface height with the reference number of 3D printed sample (reduction  $\tau/\sigma_{conf}$  can be observed when we use samples plotted with the solid symbols). Note: the physical meaning of changing variables to the fractal dimension and the standard deviation is also explained.

dilation/compaction.<sup>5,21,22</sup> Furthermore, by dividing this volume change by the area of fracture, the increase/decrease of mean fracture aperture (mechanical aperture) can be estimated. The syringe pump can control flow rates to a resolution of  $1.67 \times 10^{-5} \text{ cm}^3/\text{s}$  rendering the resolution of the calculated change in mean aperture to be comparable to that measured by LVDT.

We first conduct shearing experiments on the 9 fractured samples with defined rough surfaces. In a series of experiments, the confining pressure ( $\sigma_{conf}$ ) and the shear velocity ( $v$ ) are set to constant values of 3 MPa and  $3 \mu\text{m/s}$ , and pore pressure is set to zero (i.e., no fluid flow). We use the recovered data to evaluate the shear strength (defined as the value obtained by dividing shear stress ( $\tau$ ) by confining pressure) and the aperture volume change associated with shear dilation ( $\Delta V$ ). Since the surface roughness is the main parameter to be explored,  $\sigma_{conf}$  is not varied and the Coulomb criterion is not evaluated. In other words, the frictional coefficient ( $\mu$ ) and the cohesion ( $C_0$ ) are not specified in this study. We explore how the responses of  $\tau/\sigma_{conf}$  and  $\Delta V$  to increasing the shear displacement depend on the initial characteristics of fracture surface roughness. To specify the locations of crushed asperities due to the perfect contacting of fracture surfaces, we observe the surface textures post-experiments. Finally, to investigate the possibility of evaluating hydraulic characteristics by using the 3D printed samples, the concurrent measurements of  $\tau/\sigma_{conf}$  and fracture permeability ( $k$ ) during shearing is performed under a reference experimental condition (e.g.,  $\sigma_{conf} = 3 \text{ MPa}$ ,  $v = 3 \mu\text{m/s}$ ) for the one representative fractured sample (#5 in Fig. 1a) The inlet pore pressure is set to a constant value of 0.3 MPa and the outlet is at atmospheric ( $\sim 0.1 \text{ MPa}$ ) representing a near constant differential pressure of  $\sim 0.2 \text{ MPa}$ . Since flow rate is continuously recorded, we evaluate fracture permeability from Darcy’s law and

aperture evolution based on the cubic law assumption<sup>3</sup> assuming steady state and obviating the need to consider storage effects. The gouge/wear materials that were produced were not measured or analyzed during the fluid-flow experiments.

### 3. Experimental results and discussions

#### 3.1. Shear strength of 3D printed fractures

We summarize the experimental results of the relationship between the shear strength (defined by  $\tau/\sigma_{conf}$  in the present study), and the shear displacement of the 3D printed fractured samples in Fig. 3, where fractal dimensions of the fracture surfaces are set to 1.1 (Figs. 3a), 1.3 (Fig. 3b), and 1.5 (Fig. 3c). In Fig. 3a–c, the shear strength increases rapidly with almost no change of shear displacement. This behavior may be attributed to the difference in the stiffness/ductility between 3D printing material and rock.<sup>14,16</sup> Reduction of  $\tau/\sigma_{conf}$  with fracture shearing is observed for 5 out of the 9 printed samples and these 5 samples are plotted in Fig. 1c with the solid symbols. We find that the reduction of  $\tau/\sigma_{conf}$  (i.e., presence of peak  $\tau/\sigma_{conf}$  value) mainly results from the large magnitude of the standard deviation of fracture surface height ( $s$ ) ( $s$  is larger than 0.4 mm) and that the magnitude of fractal dimension has little influence on the presence of the peak value of  $\tau/\sigma_{conf}$ . The location of the peak  $\tau/\sigma_{conf}$  value become more ambiguous for smoother fracture surfaces. This observation for the 3D printed fractures is consistent with that of fractures in brittle rock simulants.<sup>8</sup> We suspect that this response is related to the specific distribution of wear products that develop in “lubricating” the deformation of the fracture – whose distribution is quite sensitive to the specifics of the asperity failure process (size of

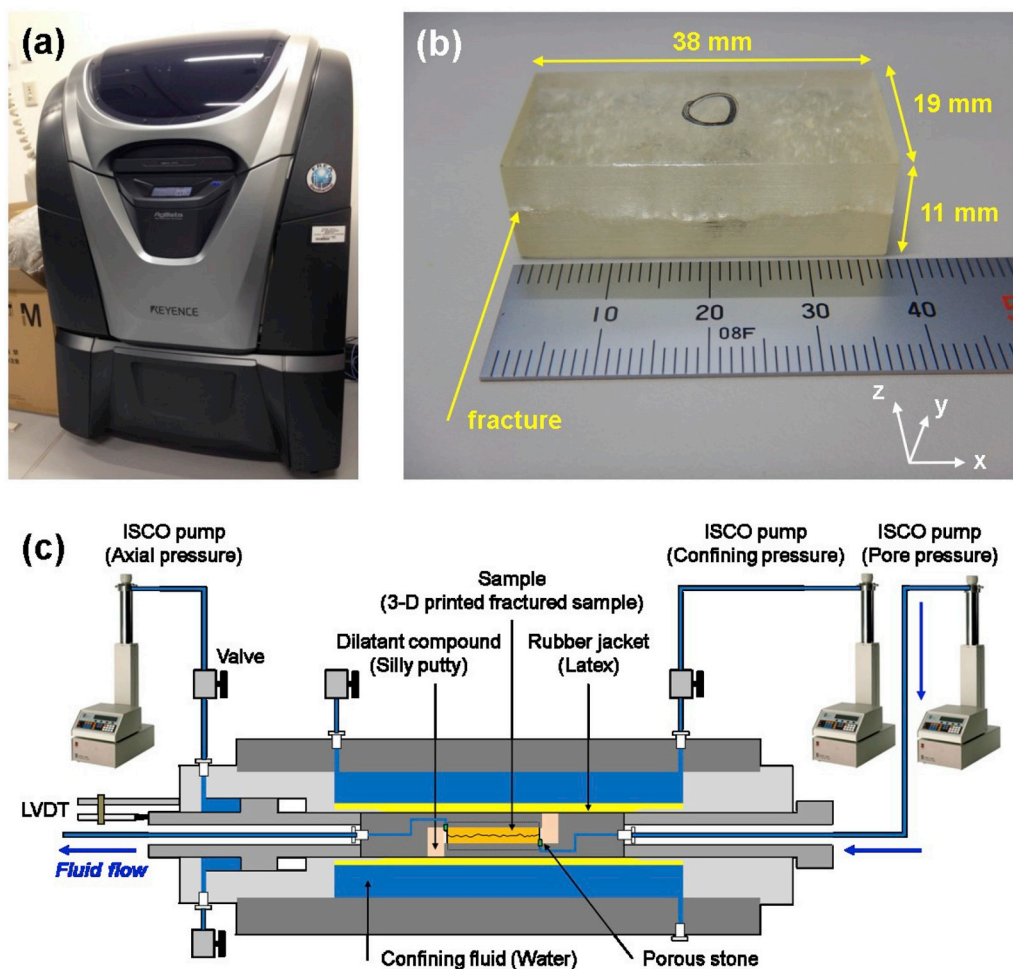


Fig. 2. (a) 3D printer used in preparing fracture samples with controlled roughness (AGLISTA-3100, Keyence), (b) Pair of 3D printed fractured samples, and (c) Experimental configuration for concurrently measuring the strength and fracture permeability of the 3D printed mated fracture pairs.

**Table 2**  
Physical properties of acrylic resin used in the 3D printing.

Properties	Values	Units
Tensile strength	40–55	MPa
Young’s modulus	1800–2100	MPa
Elongation at break	5–35	%
Flexural strength	60–80	MPa
Flexural modulus	1900–2400	MPa
Compressive strength	70–80	MPa
Izot notched impact	1.7–2.1	kJ/m2
Rockwell hardness	119–122	–
Glass transition temperature	77–80	°C

asperity removed and then its communication and distribution).

Subsequently, the dependency of representative parameters on  $s$  and  $D$  is evaluated (see Fig. 3 for their definitions). First, we find that both peak strength and post-peak strength tend to increase with increasing  $s$  (Fig. 3d) – this is principally due to the difference in the contact area of the fracture. Since the fracture surface area increases with  $s$  value, the sum of true-contact area also increases and works as the resistance to the shear. This experimental result is consistent with previous studies of shear strength for rock fractures<sup>8,22</sup> and suggests the potential of using the 3D printed artificial fractures as an alternative to natural rock fractures. Moreover, we also find that the displacement at peak strength tends to decrease with increasing  $D$  (Fig. 3e), which is caused by the change in the dominant waveform relevant to the fracture surface geometry. For instance, when comparing the representative scan lines of

samples #5 and #7 in Fig. 1b, their difference is distinguishable and the short wavelength becomes dominant with increasing  $D$ . Since the 3D printing technique enables accurate replication of even subtle differences in the surface topography, this enables the construction the more precise descriptions between roughness parameters and the hydromechanical properties of rock fractures.

### 3.2. Dilatation/compaction, surface deformation, and permeability of 3D printed fractures

Experimental results linking aperture volume change ( $\Delta V$ ) and the aperture change ( $\Delta e$ ) associated with shear dilatation and shear displacement of the 3D printed fractured samples are shown in Fig. 4. A constant fractal dimension of 1.1 is set in Fig. 4a and a constant standard deviation of 0.4 mm is set in Fig. 4b. In Fig. 4a and b, the positive values of  $\Delta V$  and  $\Delta e$  correspond to the fracture dilatation behavior, while negative values correspond to the fracture compaction.

Regardless of the  $s$  and  $D$  values, compaction always occurs prior to dilatation during fracture shearing (e.g., between 0 mm and 1.0 mm in Fig. 4). In addition, the rate of change of aperture volume change to the shear displacement gradually decreases and approaches a constant value with fracture shearing. These behaviors are consistent with observations in experiments with real rock fractures.<sup>5,6,23</sup> Note that the two facing fracture surfaces are bedded-in and interlocked at the beginning of shearing. Thus, an initial short shear deformation is recognized to be essential for the fracture to rise over the asperities encountered at the initiation of shear.

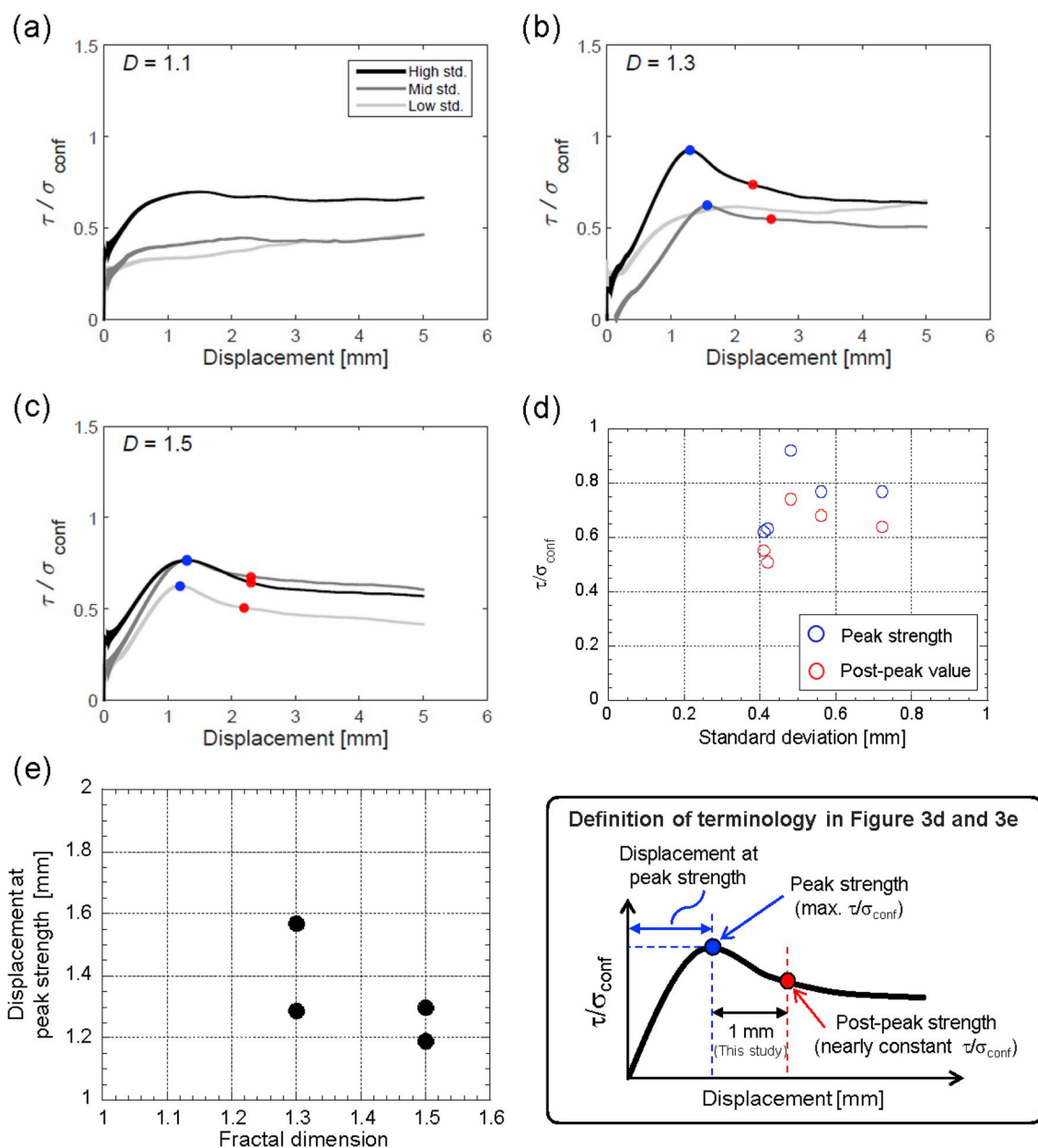


**Fig. 3.** Experimental results showing shear strength versus shear displacement for the 3D printed fracture samples with fractal dimensions of (a) 1.1, (b) 1.3, and (c) 1.5. The peak values of shear strength are plotted in blue, and the post peak values plotted in red. Based on these results, we show (d) changes in the peak shear strength and the post-peak shear strength with the standard deviation of fracture surface height and (e) change in the length necessary to achieve the peak shear strength with the fractal dimension. (For interpretation of the references to colour in this figure legend, the reader is referred to the Web version of this article.)

The aperture volume change and the associated aperture change increase with an increase in the standard deviation of fracture surface height (Fig. 4a) but are only minimally affected by an increase in fractal dimension (Fig. 4b). This result suggests that the dilation rate is mainly controlled by the average amplitude of the long period wavelength of the fracture surface and is little influenced by the minor amplitude roughness (of some tens of microns). In contrast, these microscale asperities are easily detached from the fracture surface and contribute to the production of granular wear products and in smoothing the underlying surface.<sup>2,5</sup> The change in fracture aperture is on the order of several hundred microns and is comparable to the standard deviation of the fractures surface height – since the series of experiments is conducted under a relatively low stress state (i.e.,  $\sigma_{conf} = 3$  MPa). The aperture  $\Delta e$  first decreases (compacts) with increasing stress and then stabilizes.<sup>5,6,8</sup> A representative surface state of a 3D printed fracture

post-shearing is shown in Fig. 4c, where only a limited part of the surface is damaged and is clearly marked with wear products (see the areas surrounded by dashed line in Fig. 4c). These damaged areas function as true-contacting asperities and are directly involved in the shear resistance/shear dilation. Interestingly, the damaged areas correspond to the areas where the height difference of the fracture surface changes most rapidly (steepest). This observation is essential in exploring the strict relationship between the surface roughness, the shear strength, and the stress drop of rock fractures.<sup>1,4,10</sup>

Finally, we explore the permeability evolution of a 3D printed fracture in response to shearing (Fig. 5) where the evolutions of  $\tau/\sigma_{conf}$  and the remaining volume of the syringe pump are superimposed. While the mechanical and geometrical properties of porosity and fracture network architecture have been often evaluated in 3D printed samples,<sup>11–13,15</sup> their hydraulic properties are rarely explored. As apparent in Fig. 5, the

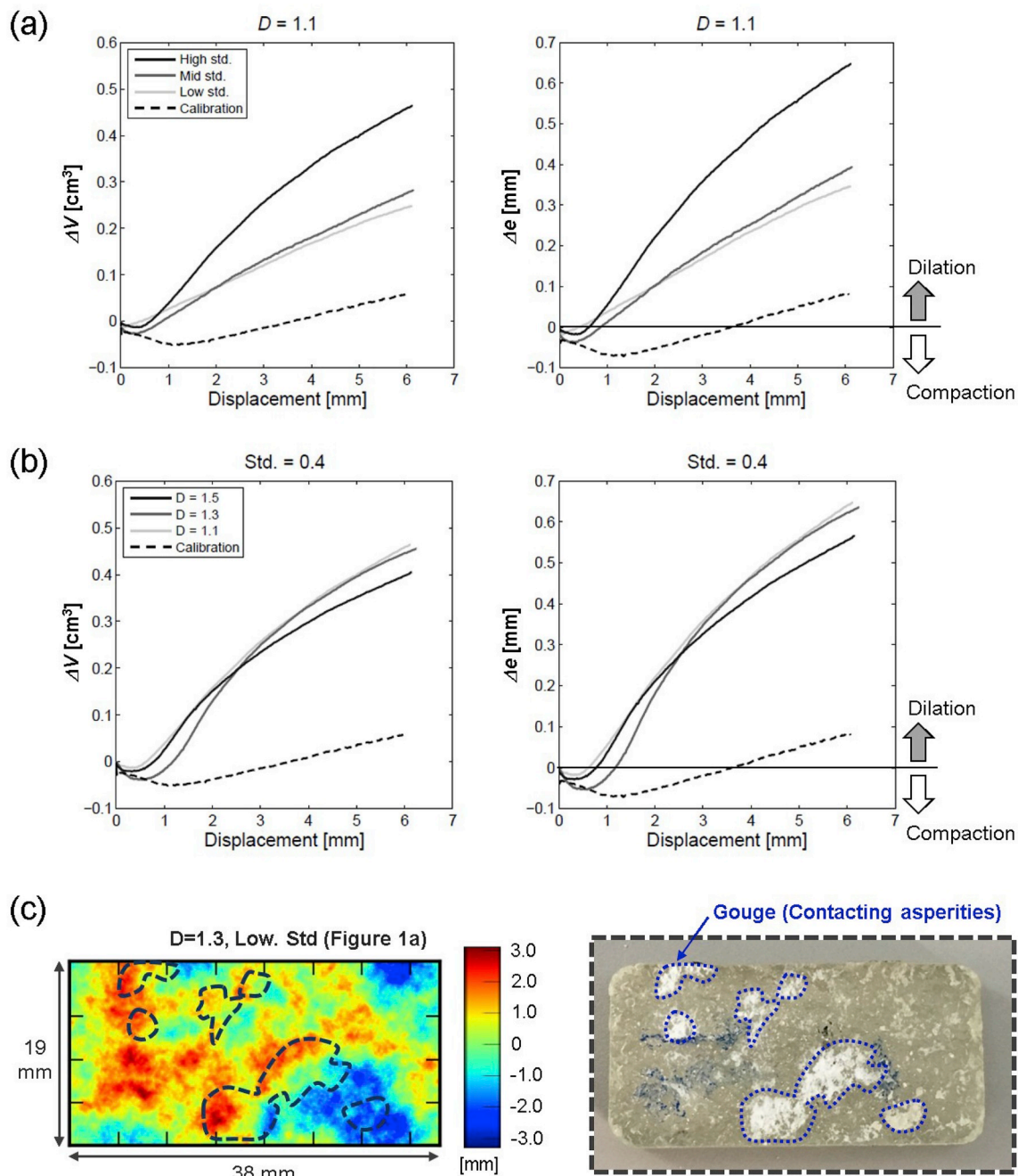


**Fig. 4.** Aperture volume change associated with shear dilation and the change in the averaged mean aperture with increasing shear offset of fractures. These values are calculated based on the remnant volume in the syringe pump used to apply the constant confining stress. These changes are evaluated for fractures with (a) constant fractal dimension of 1.1 or (b) nearly constant standard deviation of 0.4 mm. In addition, the surface state of the 3D printed fracture post-experiment is shown in Fig. 4c, it is apparent that only a limited part of the surface is damaged.

permeability of 3D printed fractures is of the order of  $10^{-10}$  m<sup>2</sup> under a confining stress of 3 MPa. This compares favorably with the permeability of rough granite fractures as  $4.3 \times 10^{-10}$  m<sup>2</sup> to  $6.3 \times 10^{-10}$  m<sup>2</sup> under normal stresses of 1 MPa–5 MPa.<sup>5</sup> With increasing shear displacement, the fracture permeability first decreases and then transits to increase with oscillations. Although the transitional slip distance is different between real and printed samples, the overall trend of permeability change with shear slip corresponds to that of the remaining volume of syringe pump – reflecting the change in mechanical aperture. The reduction of the fracture permeability is caused by the enhanced interlocking of the fracture surfaces and the consequent fracture compaction. Conversely, the permeability oscillation is possibly caused

by competition between the simultaneous dilation and associated production of gouge/wear materials. Although the ductility of asperities in the acrylic resin is generally higher than that of real rock, we confirm that the resin asperities are indeed sheared-off and produce gouge/wear-products on the fracture surface as a consequence of shearing in the experiments. Considering the aforementioned mechanisms are both active during the shearing of real rock fractures,<sup>5,23</sup> we further suggest that 3D printed fractures provide a useful analog of real rock fracture when exploring slip-permeability coupling during shear slip.

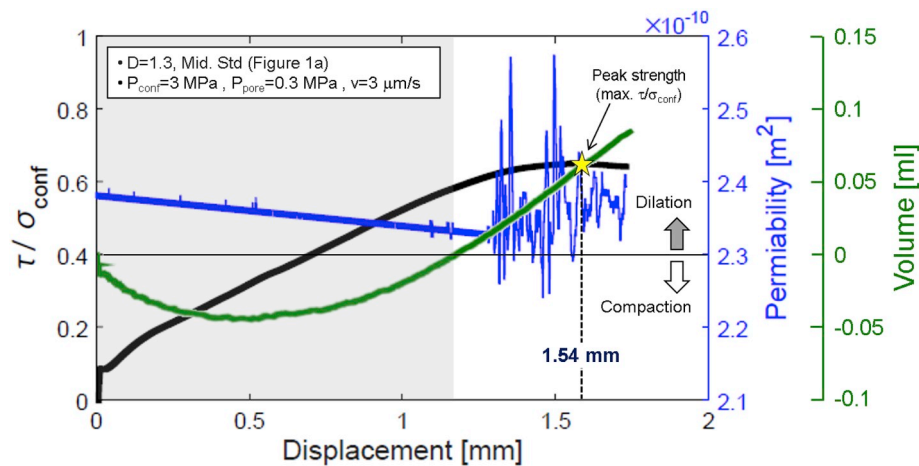


Fig. 5. Concurrent measurement of shear strength and fracture permeability of 3D printed fracture during shearing under a confining stress of 3 MPa. Change in the remnant volume within the syringe pump controlling confining stress is also shown and used to evaluate dilation/compaction of the fracture.

### 3.3. Prospects for the future researches using 3D printing technology

As described above, we demonstrate the potential of mated 3D printed fractures to explore hydromechanical coupling processes during shear slip. Since transparent resin can also be selected for the 3D printing material, 3D printing can allow direct in-situ visualization/analysis of the time-dependent deformation and breakage of asperities by coupling with appropriate visualization techniques. This offers the potential to revisit the contributing and controlling physical processes implicated in various deformation models,<sup>8</sup> that has been difficult to explore with conventional casting techniques using mortar or plaster.

In contrast, Abe et al. (2019)<sup>24</sup> suggest the potential of 3D printed samples to study fracture propagation and the interaction between hydraulic fractures and preexisting fractures. In addition, 3D printing techniques enables the design and creation of complex fracture networks with specified fracture size distributions and specified aperture distributions that may be repeated<sup>12</sup> – a feature not possible in real rock. Therefore, 3D printing provides a promising method in exploring hydraulic fracturing experiments with specified complex fracture network, and would provide useful datasets for verification of hydraulic fracturing simulators.

## 4. Conclusion

We evaluate mechanisms of hydromechanical coupling between shear strength and permeability for 3D printed fractures with systematically controlled surface roughness. 3D printing is capable of preparing repeatable fractures with a specified surface roughness in both wavelength and amplitude. Our results confirm the possibility of using 3D printed fractures as an analog to real rock fractures to explore hydromechanical coupling in rock fractures. Importantly, the printed fractures can represent the following subtle behavioral trends: (1) Shear strength increases with increasing the standard deviation of the surface height, (2) Compactive-dilatative behavior is controlled by the long-wavelength characteristics of surface roughness, and (3) With increasing shear displacement, fracture permeability first decreases and then increases with sharp oscillations controlled by the realignment of fracture-fracture contact architecture. Thus, once guided by an appropriate approach, 3D printing provides an innovative tool for the geo-engineering studies.

### Declaration of competing interest

The authors declare that they have no known competing financial interests or personal relationships that could have appeared to influence the work reported in this paper.

## Acknowledgement

The authors thank Satoru Ishikawa for his contribution to the data analysis. The authors thank the anonymous reviewers for their constructive suggestions. This work was performed in part in a scheme of Reconstruction Support Program in FREA. The present study was supported in part by JSPS KAKENHI Grant Number JP19K15495 (to T.I) and by METI, Japan through the International Research Program for Innovative Energy Technology (to H.A). The data to reproduce the work are available from the corresponding author: Takuya Ishibashi ([takuya.ishibashi@aist.go.jp](mailto:takuya.ishibashi@aist.go.jp)).

## Appendix A. Supplementary data

Supplementary data to this article can be found online at <https://doi.org/10.1016/j.ijrmm.2020.104271>.

## References

- 1 Brodsky EE, Kirkpatrick JD, Candela T. Constraints from fault roughness on the scale-dependent strength of rocks. *Geology*. 2015;44(1):19–22.
- 2 Fang Y, Elsworth D, Ishibashi T, Zhang F. Permeability evolution and frictional stability of fabricated fractures with specified roughness. *J Geophys Res: Solid Earth*. 2018;123. <https://doi.org/10.1029/2018JB016215>.
- 3 Ishibashi T, Watanabe N, Hirano N, Okamoto A, Tsuchiya N. Beyond-laboratory-scale prediction for channeling flows through subsurface rock fractures with heterogeneous aperture distributions revealed by laboratory evaluation. *J Geophys Res*. 2015;120. <https://doi.org/10.1002/2014JB01555>.
- 4 Zielke O, Galis M, Mai PM. Fault roughness and strength heterogeneity control earthquake size and stress drop. *Geophys Res Lett*. 2017;44:777–783. <https://doi.org/10.1002/2016GL071700>.
- 5 Esaki T, Du S, Mitani Y, Ikusada K, Jing L. Development of a shear-flow test apparatus and determination of coupled properties for a single rock joint. *Int J Rock Mech Min Sci*. 1999;36:641–650.
- 6 Olsson R, Barton N. An improved model for hydromechanical coupling during shearing of rock joints. *Int J Rock Mech Min Sci*. 2001;38:317–329.
- 7 Park J-W, Lee Y-K, Song J-J, Choi B-H. A Constitutive model for shear behavior of rock joints based on three-dimensional quantification of joint roughness. *Rock Mech Rock Eng*. 2013;46:1513–1537.
- 8 Barton N, Bandis S, Bakhtar K. Strength, deformation and Conductivity coupling of rock joints. *Int J Rock Mech Min Sci*. 1985;22(3):121–140.
- 9 Maini YNT. *In-situ Hydraulic Parameters in Jointed Rock – Their Measurement and Interpretation*. Ph. D. thesis. Univ. of London, Imp. Coll. of Sci. and Technol; 1971.
- 10 Candela T, Renard F, Bouchon M, Schmittbuhl J, Brodsky EE. Stress drop during earthquakes: effect of fault roughness scaling. *Bull Seismol Soc Am*. 2011;101(5):2369–2387. <https://doi.org/10.1785/0120100298>.
- 11 Head D, Vanorio T. Effects of changes in rock microstructures on permeability: 3-D printing investigation. *Geophys Res Lett*. 2016;43:7494–7502. <https://doi.org/10.1002/2016GL069334>.
- 12 Suzuki A, Watanabe N, Li K, Horne RN. Fracture network created by 3-D printer and its validation using CT images. *Water Resour Res*. 2017;53:6330–6339. <https://doi.org/10.1002/2017WR021032>.

- 13 Ishutov S, Hasiuk FJ, Jobe D, Agar S. Using resin-based 3D printing to build geometrically accurate proxies of porous sedimentary rocks. *Groundwater*. 2018;56: 482–490. <https://doi.org/10.1111/gwat.12601>.
- 14 Zhou T, Zhu JB. Identification of a suitable 3D printing material for mimicking brittle and hard rocks and its brittleness enhancements. *Rock Mech Rock Eng*. 2018;51: 765–777.
- 15 Vogler D, Walsh SDC, Dombrowski E, Perras MA. A comparison of tensile failure in 3D-printed and natural sandstone. *Eng Geol*. 2017;226:221–235.
- 16 Kong L, Ostadhassan M, Li C, Tamimi N. Can 3-D printed gypsum samples replicate natural rocks? An experimental study. *Rock Mech Rock Eng*. 2018;51:3061–3074.
- 17 Liu P, Ju Y, Ranjith PG, Zheng Z, Wang L, Wanniarachchi A. Visual representation and characterization of three-dimensional hydrofracturing cracks within heterogeneous rock through 3D printing and transparent models. *Int J Coal Sci Technol*. 2016;3(3):284–294.
- 18 Brown SR. Simple mathematical model of a rough fracture. *J Geophys Res*. 1995;100 (B4):5941–5952. <https://doi.org/10.1029/94JB03262>.
- 19 Glover PWJ, Matsuki K, Hikima R, Hayashi K. Synthetic rough fractures in rocks. *J Geophys Res*. 1998;103(B5):9609–9620. <https://doi.org/10.1029/97JB02836>.
- 20 Power WL, Tullis TE, Brown SR, Boitnott GN, Scholz CH. Roughness of natural fault surfaces. *Geophys Res Lett*. 1987;14(1):29–32. <https://doi.org/10.1029/GL014i001p00029>.
- 21 Goodman RE. *Methods of Geological Engineering in Discontinuous Rocks*. St Paul: West Publishing Company; 1976:472.
- 22 Barton N. Shear strength criteria for rock, rock joints, rockfill and rock masses: problem and some solutions. *J Rock Mech Geotech Eng*. 2013;5:249–261.
- 23 Javadi M, Sharifzadeh M, Shahriar K, Mitani Y. Critical Reynolds number for nonlinear flow through rough-walled fractures: the role of shear process. *Water Resour Res*. 2014;50:1789–1804.
- 24 Abe A, Ishibashi T, Asanuma H, Horne RN. Numerical modeling and laboratory experiments on a propagating hydraulic fracture intersecting with a preexisting fracture. In: *Proc 43<sup>rd</sup> Workshop On Geothermal Reservoir Engineering*. 2019. SGP-TR-214.